Optics Letters

Focused vortex beam generator suitable for optical fiber spanners in a complex liquid environment

Zhiyong Bai,[1,2] Luping Wu,[1,2] Rui Liu,[1,2] Jian Yu,[1,2] Dingbang Ma,[1,2] Zikai Chen,[1,2] Jianjun Ran,[1,2] Ying Wang,[1,2] Changrui Liao,[1,2] and Yiping Wang[1,2,*]

[1]Key Laboratory of Optoelectronic Devices and Systems of Ministry of Education and Guangdong Province, College of Physics and Optoelectronic Engineering, Shenzhen University, Shenzhen 518060, China
[2]Shenzhen Key Laboratory of Photonic Devices and Sensing Systems for Internet of Things, Guangdong and Hong Kong Joint Research Center for Optical Fiber Sensors, Shenzhen University, Shenzhen 518060, China
*Corresponding author: ypwang@szu.edu.cn

Received 6 June 2022; revised 17 November 2022; accepted 17 November 2022; posted 17 November 2022; published 14 December 2022

We experimentally demonstrated an all-fiber focused vortex beam (FVB) generator which was prepared by milling a spiral zone plate (SZP) on the Au-coated end face of a hybrid fiber by focused ion beam (FIB). In this generator, the fundamental modes propagating in the hybrid fiber are focused while being modulated into high-order orbital angular momentum (OAM) mode by the SZP at the end face. The focus length and topological charge were designed and then were both theoretically and experimentally verified. The results show that, the obtained characteristics of the FVB agree with the designed ones. The measured diameters of the focal spots are 2.2 μm, 4.4 μm, and 5.2 μm for the FVB with the topological charge of 0, 1, and 2, respectively. The simulated results show that the proposed FVB generators can maintain good focusing characteristics in different liquids, so it is a good candidate for optical fiber spanner use in a complex liquid environment. Moreover, the processing efficiency of the proposed FVB generators is nearly ten times higher than that of the previously reported ones due to the Au-coated film.

https://doi.org/10.1364/OL.465949

A focused vortex beam (FVB) is regarded as an optical spanner [1,2] which provides an angular torque in optical manipulation and has been applied to micromotors [3,4], particle screening [5], and microbial molecular dynamics study [6,7]. Usually, an FVB is obtained by focusing the structural beam modulated by a spatial light modulator (SLM) through a high numerical aperture objective lens [8]. However, these are bulky and suffer from a lack of flexibility and integrability, poor remote operating capabilities, and have a high cost and requirement for infrastructure. Optical fiber opens the possibility of addressing the above-mentioned limitations and represents a flexible, large operating space, and low-cost optical tool [9–11]. Recently, several fiber-based methods have been proposed to achieve FVB. Leite *et al*. designed and prepared a kind of fiber with a high numerical aperture to transmit the structured light by an SLM and obtain multiple diffraction focuses due to the high refractive index difference of the fiber core and cladding; this method presents good flexibility in particle manipulation [12]. But this kind of specially designed optical fiber is difficult to obtain, which limits its application to some extent. Spiral zone plates (SZPs) can be used as a diffraction optical element to study the characteristics of structural beams and their interaction with matter because they can simultaneously regulate and focus the light field. Yu *et al*. achieved the generation of FVB by etching an SZP on the end face of a standard fiber [13,14]. Due to the advantages of directly generating an FVB under the wide bandwidth of incident light and its high integration with optical fiber, the generator is expected to be a good candidate for optical spanners. However, this kind of optical spanner can only be used in a single specific liquid environment. When the refractive index of the solution carrying particles changes, the generation and focusing of the vortex beam will be severely degraded or even invalidated.

In order to obtain a stable and robust FVB which can be applied to a variety of complex liquid environments, we designed and fabricated a new FVB generator. The generator is prepared by milling an SZP on the Au-coated end face of a fiber by focused ion beam (FIB). Figure 1 is the schematic diagram of the all-fiber FVB generator. This generator consists of a section of single-mode fiber (SMF) used to transmit input light, a section of graded index multimode fiber (GIMF) used to expand the mode field area [15], and an SZP to generate the FVB [16,17].

The SZP is a diffractive optical element used to directly generate an FVB, which can be regarded as a hybrid optical element combining a Fresnel zone plate (FZP) and a spiral phase plate (SPP). The phase functions of an SPP and FZP can be expressed as:

$$\mathrm{SPP}(r,\Phi) = \exp(ip\Phi) \tag{1}$$

$$\mathrm{FZP}(r,\Phi) = \exp\left(\frac{-i\pi r^2}{\lambda f}\right), \tag{2}$$

where (r,Φ) is the polar coordinate, p is the topological number equal to the number of spiral arms of the SZP, λ is the wavelength of input light in free space, and f represent the focal length. The phase function of the SZP can be expressed as follows by the combination of expressions (1) and (2):

$$\mathrm{SZP}(r,\Phi) = \exp\left(ip\Phi - \frac{i\pi r^2}{\lambda f}\right). \tag{3}$$

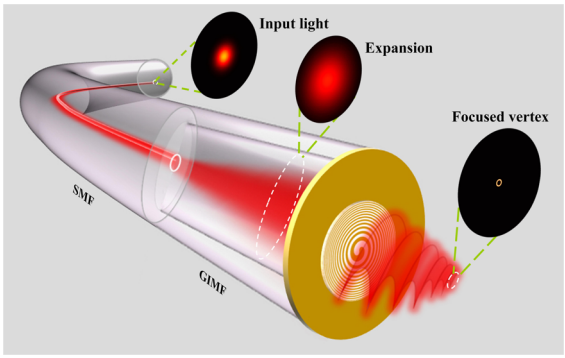

Fig. 1. Schematic diagram of the FVB generator.

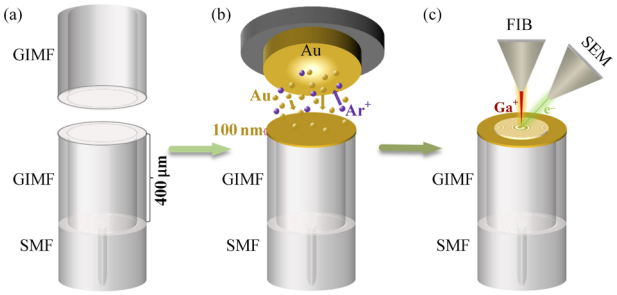

Fig. 2. Generator preparation flow chart: (a) length of GIMF is kept to 400 μm; (b) fiber end face is coated with a 100-nm Au film; (c) SZP is milled on the fiber end face by FIB.

Therefore, the binary transmittance function of the SZP was governed by the following formulas:

$$t(r,\Phi)=\begin{cases}0,\ (2k-1)\pi \le p\Phi-\dfrac{\pi r^2}{\lambda f}\le 2k\pi\\ 1,\ 2k\pi \le p\Phi-\dfrac{\pi r^2}{\lambda f}\le (2k+1)\pi\end{cases}\quad (4)$$

$$k=0,\pm 1,\pm 2\ldots.$$

For the fundamental mode beam passing through the SZP, the diffracted light of multiple zones is superimposed on the optical axis to form a focus, and the spiral zone makes the light wave reaching the focal plane have a phase difference in the angular direction to form an optical vortex [17].

The preparation process of the generator is shown in Fig. 2. Following the theories and test methods mentioned by Yu *et al.* in Ref. [14], a 400-μm length of GIMF is used to achieve output beam expansion and collimation, and maintain the fundamental mode, as shown in Fig. 2(a). In Fig. 2(b), The 100-nm Au film was coated on the end face of the GIMF by the magnetron sputtering coating system to ensure the fabrication efficiency and light field modulation efficiency of the generator. Then, the binary bitmaps were generated according to Eq. (4) and directly imported into the FIB (Nova Nano-lab 600 FEI) processing system. The focused Ga + ion beam milled the designed pattern on the coated-fiber end face, and the electron beam of the FIB system was used for imaging, as show in Fig. 2(c). It is worth mentioning that because the Au film is very thin, it took only 3.7 min to process an SZP. For $p=0$, 1, and 2, the designed patterns are shown in Figs. 3(a)–3(c), respectively, with an operation wavelength λ =1550 nm, a designed focal length $f_d=20$ μm, and an SZP diameter of 60 μm which completely covers the

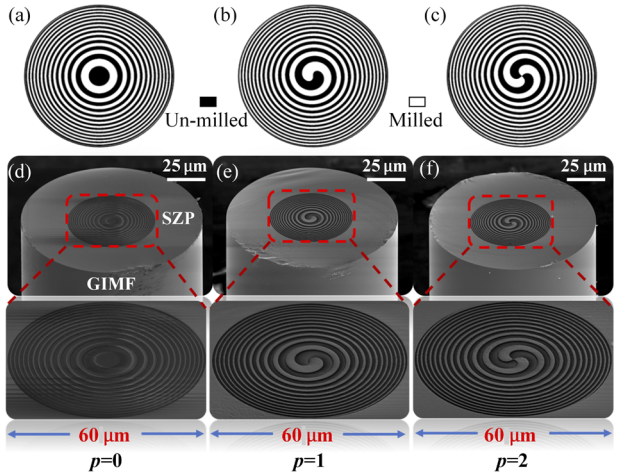

Fig. 3. Designed and SEM images of SZPs: (a)–(c) designed bitmaps with $p=0$, 1, and 2, respectively; (d)–(f) corresponding SEM images. The insets are the partially enlarged views.

light field emitted from the end face of the GIMF. The white area is the milled part and the black area is the un-milled part. Figures 3(d)–3(f) show the SEM images of the SZPs seen obliquely above, which were prepared at a beam current of 3 nA and an accelerating voltage of 30 kV. The dark area is the exposed quartz after milling and the light area is the Au film.

The optical behavior of the designed SZP was numerically simulated by the finite difference time domain (FDTD) method. A Gaussian beam with a central wavelength of 1550 nm was selected as the source. To ensure accuracy, the calculation meshing is set to 100 nm. The perfectly matched layer was selected to be the boundary condition to reduce the influence of the reflected light. The simulation results along the optical axis observed through a 3D monitor are shown in Figs. 4(a)–(c). The SZP was located at $z=0$. When p is 0, 1, and 2, the corresponding focal lengths are 18.2 μm, 17.6 μm, and 16.2 μm, respectively. The difference between the designed focal length and the simulated focal length is caused by the absence of higher-order terms after binarization. The intensity distributions at the focus are simulated, as shown in Figs. 4(d)–4(f), and the diameters of the focused mode field are 2.2 μm, 4.0 μm, and 4.7 μm for $p=0$, 1, and 2, respectively. When the topological charge $p\neq 0$, there is an annular intensity distribution at the focal spot, and the spot size increases with the increase of p. Figures 4(g)–4(i) display the theoretical interference diagrams of the vortex beam and a plane wave.

A measurement system was constructed to characterize the intensity distribution and phase of generators, as shown in Fig. 5. Light with a wavelength of 1550 nm from a tunable laser was collimated by a 10× objective lens and then divided into two beams by beam splitter 1 (BS1). One beam was coupled into the generator by a 20× objective lens, the other one was used as a reference beam. After being magnified by two 40× objective lenses, the two beams met and interfered at the second beam splitter, BS2, and the intensity distribution and interference patterns were observed using an infrared CCD. As seen in Fig. 5, polarizer 1 (P1) was jointly used to adjust polarization states of the input light. The linear polarization of the reference light is obtained by polarizer 2 (P2). A half-wave plate (HWP) was then used to rotate the linear polarization direction of the reference beam.

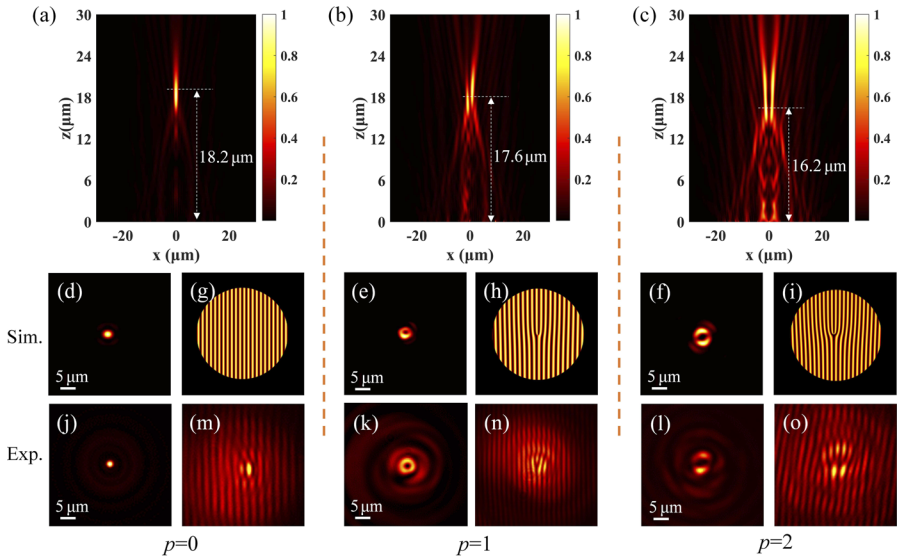

Fig. 4. (a)–(c) Normalized intensity distribution of the light beam emitted by the SZP with $p = 0$, 1, and 2, respectively; (d)–(f) and (j)–(l) simulated and measured intensity distribution, respectively, in the corresponding focusing transverse section; (g)–(i) and (m)–(o) simulated and measured interference patterns, respectively, between the corresponding focal spot and an extended Gaussian beam.

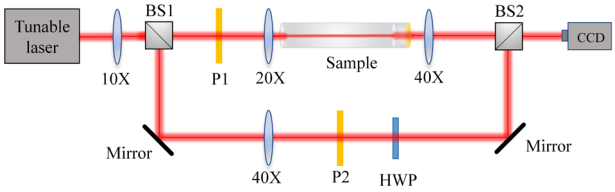

Fig. 5. Schematic diagram of the experimental setup used for detecting the characteristics of the generator.

When the reference beam was blocked by a diaphragm, the intensity distribution of the FVB could be obtained directly by the CCD as shown in Figs. 4(j)–4(l). The measured diameters of the focal spot are 2.4 μm, 4.4 μm, and 5.2 μm for SZPs with $p = 0$, 1, and 2, respectively, which is almost consistent with the simulation results. The helical phase was analyzed by the image of the interference between the output light of the generator and the reference light as shown in Figs. 4(m)–4(o). Comparing these with the simulation results, it confirms that the output focused beams from the SZPs carry orbital angular momentum (OAM). The number of forks represents the vortex topological charge number.

As shown in Fig. 6, we tested the evolution of the intensity distribution of the output light from the generator propagating along the optical axis, adjusting the distance between generator and 40× objective lens until the spot size in the CCD was the smallest. This position of the generator is regarded as the origin position (0 μm). When $p = 0$, the intensity distribution is a spot at the origin position as shown in Fig. 6(a). This shows that there are always bright spots in the middle of the intensity distribution in the negative direction away from the original position. In contrast, in the positive direction, there are always dark spots in the middle of the intensity distribution. When p is 1 or 2, there is a dark spot in the middle of the intensity distribution at the original position, as shown in Figs. 6(b) and 6(c). The intensity distribution pattern rotates counterclockwise in the negative direction and clockwise in the positive direction away from the original position. The evolution of the intensity

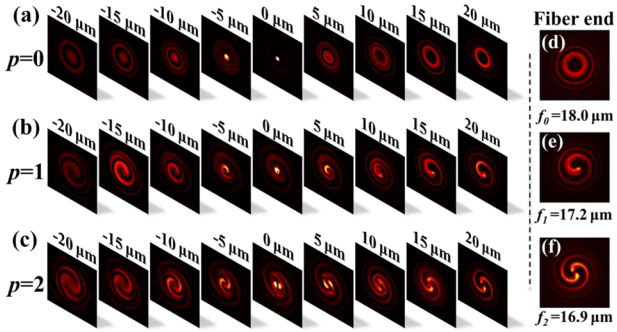

Fig. 6. (a)–(c) Light intensity distributions near the focus spot of the generators with $p = 0$, 1, and 2, respectively; (d)–(f) corresponding images of the SZP at the end of the optical fiber captured by infrared CCD.

distribution confirms the focusing characteristics of the output light from the generator.

To test the focus length of the SZP, the distance between the generator and the 40× objective lens is adjusted to find the clearest contour of the SZP on the end face of the GIMF, and this distance is then the measured focal length of the generator. For the SZP with a different number of spiral arms, the measured actual focal length values are different, as is shown in Figs. 6(d)–6(f). The focal length $f_0 = 18.0$ μm for $p = 0$, $f_1 = 17.2$ μm for $p = 1$, and $f_2 = 16.9$ μm for $p = 2$. The measured focal lengths are almost consistent with the results of the simulation. It is particularly noteworthy that there is a difference between the measured and the simulated focal length of the SZP, which may result from diffraction of the evanescent fields inside the subwavelength features of the SZP and machining measurement error of experiment.

In order to further study the focusing characteristics of the generator in different liquids, we simulated the axial distribution of the output light from the designed SZP in air, water, and glycerol, respectively. For comparison, we performed the same simulation calculation for the previously reported phase-type

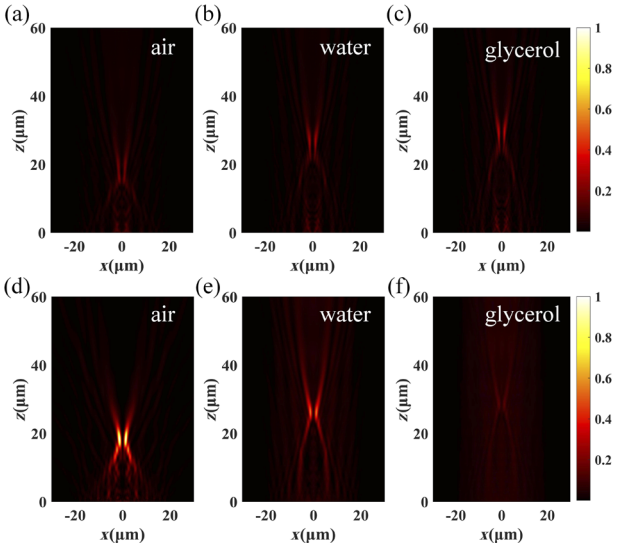

Fig. 7. Simulation of focusing characteristics of the designed SZP and phase-type SZP with $p = 2$. Axial light field distribution of (a)–(c) the designed SZP, and (d)–(f) a phase-type SZP in air, water, and glycerol, respectively. Normalization is performed by using the maximum intensity of the output light from both types of SZP.

SZP. The phase SZP is equivalent to directly milling the SZP on the hybrid fiber end face without Au film, and the thickness of the SZP is set to 1.582 μm for a better focusing characteristic in air [14]. The refractive indices of air, water, and glycerol are 1, 1.33, and 1.47, respectively. As shown in Figs. 7(a)–7(c), the focus characteristics of the proposed FVB generator with $p = 2$ is always maintained in air, water, and glycerol, and the focal length of the generator increases with the increase of environmental refractive index. In addition, by monitoring the change of power in the simulation, the transmissivity of the designed SZP in air, water, and glycerol is 46%, 45%, and 49%, respectively, and the required output power of the spanners can be easily achieved by increasing the power of the light source. Although the transmittance of the phase SZP is above 80% in different environments, the focusing pattern is significantly degraded when the surrounding environment changed from air to liquid, especially in glycerol—whose refractive index is close to that of the core material—where the generator presented a weak focus, as shown in Figs. 7(d)–7(f). The reason for this is that the glycerol fills the milled part of SZP and destroys the phase modulation, and as a result, the diffraction focusing cannot be realized. Therefore, the numerical results show that the amplitude-type FVB generator proposed in this work always maintains the focusing characteristic of the beam in the liquid environment with variable refractive index. It is worth noting that the generator can be reused after direct ultrasonic cleaning.

In conclusion, we have fabricated an SZP on an Au-coated end face of GIMF fused with a section of SMF to generate an FVB. The intensity distribution, focusing characteristics, and phase information of the vortex beam excited by the generator have been investigated theoretically and experimentally. The experimental results are in good agreement with the theoretical ones. The generator can directly excite an FVB, which indicates a natural optical spanner. Combined with the operational flexibility of optical fiber, it can be used in device tubes, such as blood vessels, for cell manipulation.

Funding. National Natural Science Foundation of China (61875134, 62005169); Natural Science Foundation of Guangdong Province (2022A1515010183); Foundation of Shenzhen University (201904).

Acknowledgments. The authors wish to acknowledge the assistance on FIB received from the Electron Microscope Center of Shenzhen University.

Disclosures. The authors declare no conflicts of interest.

Data availability. Data underlying the results presented in this paper are not publicly available at this time but may be obtained from the authors upon reasonable request.

REFERENCES

1. N. B. Simpson, K. Dholakia, L. Allen, and M. J. Padgett, Opt. Lett. **22**, 52 (1997).
2. K. Dholakia and T. Čižmár, Nat. Photonics **5**, 335 (2011).
3. A. B. Stilgoe, T. A. Nieminen, and H. Rubinsztein-Dunlop, Nat. Photonics **16**, 346 (2022).
4. S. Zhang, L. J. Gibson, A. B. Stilgoe, I. A. Favre-Bulle, T. A. Nieminen, and H. Rubinsztein-Dunlop, Optica **4**, 1103 (2017).
5. A. E. Carruthers, J. S. Walker, A. Casey, A. J. Orr-Ewing, and J. P. Reid, Phys. Chem. Chem. Phys. **14**, 6741 (2012).
6. M. Kreysing, D. Ott, M. J. Schmidberger, O. Otto, M. Schürmann, E. Martín-Badosa, G. Whyte, and J. Guck, Nat. Commun. **5**, 5481 (2014).
7. H. Xin, N. Zhao, Y. Wang, X. Zhao, T. Pan, Y. Shi, and B. Li, Nano Lett. **20**, 7177 (2020).
8. N. Bhebhe, P. A. C. Williams, C. Rosales-Guzmán, V. Rodriguez-Fajardo, and A. Forbes, Sci. Rep. **8**, 17387 (2018).
9. H. Deng, D. Chen, R. Wang, F. Li, Z. Luo, S. Deng, J. Yin, L. Yu, W. Zhang, and L. Yuan, Nanoscale **14**, 6941 (2022).
10. M. Plidschun, H. Ren, J. Kim, R. Forster, S. A. Maier, and M. A. Schmidt, Light: Sci. Appl. **10**, 57 (2021).
11. C. Guan, M. Ding, J. Shi, P. Wang, P. Hua, L. Yuan, and G. Brambilla, Opt. Lett. **39**, 1113 (2014).
12. I. T. Leite, S. Turtaev, X. Jiang, M. Šiler, A. Cuschieri, P. S. J. Russell, and T. Čižmár, Nat. Photonics **12**, 33 (2018).
13. J. Yu, C. Fu, Z. Bai, and Y. Wang, J. Lightwave Technol. **39**, 1416 (2021).
14. J. Yu, Y.-P. Wang, W. Yang, Z.-Y. Bai, Z. Xie, Z. Liu, and C.-R. Liao, Appl. Phys. Lett. **116**, 241102 (2020).
15. X. Xu, J. He, M. Hou, S. Liu, Z. Bai, Y. Wang, C. Liao, Z. Ouyang, and Y. Wang, J. Lightwave Technol. **36**, 2827 (2018).
16. A. Balčytis, D. Hakobyan, M. Gabalis, A. Žukauskas, D. Urbonas, M. Malinauskas, R. Petruškevičius, E. Brasselet, and S. Juodkazis, Opt. Express **24**, 16988 (2016).
17. H. Liu, M. Q. Mehmood, K. Huang, L. Ke, H. Ye, P. Genevet, M. Zhang, A. Danner, S. P. Yeo, C.-W. Qiu, and J. Teng, Adv. Opt. Mater. **2**, 1193 (2014).